


 Cite this: *RSC Adv.*, 2022, 12, 25578

Structural elucidation of hexavalent Cr adsorbed on surfaces and bulks of Fe₃O₄ and α-FeOOH†

 Nichapha Senamart,^a Krittanun Deekamwong,^b Jatuporn Wittayakun,^b Sanchai Prayoonpokarach,^b Narong Chanlek,^c Yingyot Poo-arporn,^c Suttipong Wannapaiboon,^c Pinit Kidkhunthod^{b,c} and Sirinuch Loiha^{b,*a}

Magnetite (Fe₃O₄) and goethite (α-FeOOH) were synthesized *via* a hydrothermal approach and utilized as adsorbents for Cr⁶⁺ removal in an aqueous medium. The typical crystal structures of the synthesized Fe₃O₄ and α-FeOOH were confirmed by XRD and TEM. Fe₃O₄ in a spherical shape with a surface area of 32 m² g⁻¹ was established. While α-FeOOH had a rod-like form with a larger surface area of 84 m² g⁻¹. Cr⁶⁺ removal in an aqueous solution was studied in various conditions to evaluate thermodynamic and kinetic parameters. The adsorption isotherms on both adsorbents fit the Langmuir model indicating monolayer adsorption. Fe₃O₄ showed a better adsorption ability than α-FeOOH even though it had a lower surface area. XAS and XPS analysis strongly evidenced the production of stable Cr³⁺ species of Fe_(1-x)Cr_xOOH and Fe_(3-x)Cr_xO₄ by Cr⁶⁺ reduction and migration processes into the bulk structure. Thus, the existence of stable Cr-species in Fe₃O₄ structure strongly affected Cr-adsorption ability rather than the surface area of the adsorbent. However, the precipitated Cr₂O₃ and HCrO₄⁻ molecules electrostatically adsorbed on the outer surface of α-FeOOH without bulk transformation. The presence of physisorbed FeO–HCrO₄ species on α-FeOOH led to low reducibility and adsorption capability of Cr⁶⁺.

 Received 16th June 2022
 Accepted 30th August 2022

DOI: 10.1039/d2ra03676b

rsc.li/rsc-advances

Introduction

Hexavalent Cr⁶⁺ ions are toxic contaminants because of their mutagenicity, carcinogenicity, and teratogenicity.^{1–5} Toxic Cr⁶⁺ species generally exist in negatively charged forms, such as the ions of hydrogen chromate (HCrO₄⁻), chromate (CrO₄²⁻), and dichromate (Cr₂O₇²⁻), depending on solution pH and concentration.^{6,7} However, no conclusive spectroscopic proof of structural changes in adsorbents and adsorbates is available.^{8,9} X-ray absorption spectroscopy (XAS) is a powerful tool for the element-specific characterization of local structure and chemistry. The electronic and local structures or geometry of chromium species in water will be explored. Understanding the stabilized Cr-species on the adsorbents is beneficial to the development of new materials from the waste treatment process. Wei *et al.*¹⁰ illustrated the determination of Cr-contamination in kitchen wastewater by XAS. The Cr-species distribution in the solution was estimated. Likewise, Meena and Arai¹¹ could explore the Cr³⁺/Cr⁶⁺ ratio and Cr-structures on

Fe₃O₄ through the Cr-adsorption process from groundwater by using X-ray absorption near edge structure (XANES) and extended X-ray absorption fine structure (EXAFS) analysis.

Different techniques, such as chemical precipitation, adsorption, photocatalysis, and reduction using cationic materials, are available for the removal of Cr⁶⁺ from wastewater.^{7,12–16} Utilization of natural-cationic materials, such as activated carbon, chitosan, chelate resins, and natural zeolites for Cr⁶⁺ adsorption has been widely investigated due to their low cost, feasibility, handling simplicity, and flexibility.^{17–20} However, the removal of the adsorbed Cr⁶⁺ species by those adsorbents still needs a further reduction process to complete the Cr disposal.

Chemical reduction using environment-friendly materials, such as iron oxides, is an interesting alternative method for Cr⁶⁺ removal from wastewater.^{21,22} Iron (oxy) hydroxide of goethite (α-FeOOH) containing Fe³⁺ is a potential Cr⁶⁺ adsorbent due to its high surface area and thermal stability.^{7,23} Moreover, octahedral sites of Fe³⁺ in orthorhombic α-FeOOH structure play a significant role in Cr⁶⁺ adsorption. In addition, the presence of a small amount of Fe²⁺ species on the α-FeOOH surface provides a great reduction potential for Cr⁶⁺ ions.²⁴ However, a drawback of polymorphs of the synthetic α-FeOOH formed in acidic conditions leads to an additional protonation, resulting in structure destabilization.^{7,25,26} Hence, the preparation of a stable α-FeOOH structure with uniform crystalline needs to be investigated. Additionally, the metal oxide of Fe₃O₄ (magnetite) or ferrous-ferric iron oxide nature is interesting for Cr⁶⁺ removal

^aCenter for Innovation in Chemistry (PERCH-CIC), Materials Chemistry Research Center, Department of Chemistry, Faculty of Science, Khon Kaen University, Khon Kaen 40002, Thailand. E-mail: sirilo@kku.ac.th

^bSchool of Chemistry, Institute of Science, Suranaree University of Technology, Nakhon Ratchasima, 30000, Thailand

^cSynchrotron Light Research Institute, Nakhon Ratchasima 30000, Thailand

† Electronic supplementary information (ESI) available. See <https://doi.org/10.1039/d2ra03676b>



because it has a suitable redox potential for Cr^{6+} reduction and excellent magnetic properties.^{27,28} It is widely known that Fe^{2+} in magnetite can reduce Cr^{6+} to Cr^{3+} creating Cr^{3+} -hydroxide or mixed substances *via* an adsorption and reduction process, namely reductive precipitation.^{29,30} This adsorption behavior on the Fe_3O_4 surface was explored and Cr^{3+} and Fe^{3+} -(oxy)hydroxides were passivated on the adsorbent surface.³⁰ The adsorption ability and structural stability of Fe_3O_4 are strongly affected by solution pH and the homogeneity of iron oxide particles. The effect of the passivation layer on bulk structure deserves our study. In addition, the relationship between adsorption ability and phase stability in bulk-iron oxides needs to be investigated. Understanding the stable Cr-forms on the ion-oxides is promising for catalyst applications.³¹

In the present study, iron oxides of Fe_3O_4 and $\alpha\text{-FeOOH}$ were synthesized by the hydrothermal method and used as Cr^{6+} adsorbents. The crystalline structure, morphology, and surface area of the bare and adsorbed materials were characterized. The Cr-adsorption ability and behavior were explored. The adsorbent surfaces and bulk structures were elucidated by XPS and XAS.

Experimental

Materials and methods

Materials. The chemicals including iron(III) nitrate nonahydrate ($\text{Fe}(\text{NO}_3)_3 \cdot 9\text{H}_2\text{O}$, 98%, Merck), iron(III) chloride (FeCl_3 , 98%, ACROS), potassium dichromate ($\text{K}_2\text{Cr}_2\text{O}_7$, 99.9%, LOBA), sodium acetate (NaOAc, 99.5%, LOBA), potassium hydroxide pellets (KOH, 85%, LOBA), hydrochloric acid (HCl, 37%, QR $\ddot{\text{e}}\text{C}^{\text{TM}}$), ethylene glycol (EG, AR grade, QR $\ddot{\text{e}}\text{C}^{\text{TM}}$) and 1,5-diphenylcabazone (50% diphenylcabazid, ACS grade, Merck) were used in this work.

Methods. The crystal structures of $\alpha\text{-FeOOH}$ and Fe_3O_4 were revealed by powder X-ray diffraction (XRD; PANalytical, EMPY-REAN). The XRD patterns were indexed by Match! Software using the Crystallography Open Database (COD), which was available at Beamline 1.1 W (Multiple X-ray Techniques), Synchrotron Light Research Institute, Thailand, SLRI. The unit cell parameters are refined by using FullProf Software. Morphologies were detected by transmission electron microscopy (TEM; Tecnai G²). The oxidation states of the samples before and after adsorption were determined by X-ray absorption spectroscopy (XAS) under the 3.2 and 5.2 beamlines (SLRI) in the intermediate photon energy ranges of Cr *K*-edge (5.7–6.7 keV), Fe *K*-edge (7.0–8.0 keV), Fe *L*₃-edge (0.7–0.73 keV) and O *K*-edge (5.2–5.5 keV), respectively. The chemical states of Fe, Cr and O were analyzed by X-ray photoelectron spectroscopy (XPS; PHI5000 Versa Probe II, ULVAC-PHI, Japan) at the SUT-NANOTEC-SLRI Joint Research Facility, 5.2 beamline.

Synthetic procedures

Synthesis of $\alpha\text{-FeOOH}$. Goethite ($\alpha\text{-FeOOH}$) was synthesized by the following hydrothermal route.³² Iron solution was prepared by dissolving 4.85 g of $\text{Fe}(\text{NO}_3)_3 \cdot 9\text{H}_2\text{O}$ into 10 mL of deionized (DI) water. The solution was then slowly dropped into 10 mL of 4.8 M KOH solution. The mixture was transferred to

a Teflon-lined autoclave and crystallized at 100 °C for 6 h. The crystallized sample was then washed with DI water and ethanol several times, and the resultant brown powder of goethite was dried overnight at 50 °C.

Synthesis of Fe_3O_4 . Magnetite (Fe_3O_4) was synthesized by the following route.³³ 1.94 g of FeCl_3 solution was dissolved into 40 mL of EG in a two-necked round-bottom flask under N_2 atmosphere. The solution mixture was stirred for 30 min and then 10 mL of 1.35 M NaOAc in EG was then added. After 3 h, the mixture was transferred to a Teflon-lined autoclave and heated to 190 °C for 24 h. The obtained powder was separated by a magnetic bar. The resultant black powder of Fe_3O_4 was washed with DI water and ethanol several times and dried overnight at 50 °C.

Cr^{6+} adsorption analysis. A stock solution of 100 ppm Cr^{6+} was prepared from $\text{K}_2\text{Cr}_2\text{O}_7$. Working solutions with desired concentrations were prepared by diluting the stock solution with DI water. Adsorption experiments were carried out by adding each adsorbent to 50 mL of Cr^{6+} solution and stirring vigorously. After adsorption, the adsorbents were separated from the solution by centrifugation for $\alpha\text{-FeOOH}$ and using a magnet for Fe_3O_4 . Cr^{6+} concentrations were determined by the colorimetric method. Each sampling solution was added to 1,5-diphenylcabazone ligand with 10% (v/v) of H_2SO_4 (pH = 2) to form chromium complex. The absorbance of this complex was collected by using UV-Vis spectrophotometry at $\lambda_{\text{max}} = 540 \text{ nm}$.^{34,35} The Cr adsorption capacity of the adsorbents (mg g^{-1}) was calculated as

$$\text{Adsorption capacity } (q_e) = \frac{(C_0 - C_e)}{W} V,$$

where C_0 (mg L^{-1}) and C_e (mg L^{-1}) are the initial and equilibrium metal concentrations, respectively, V (L) is the solution volume, and W (g) is the adsorbent weight.

Adsorption isotherms were detected by the Langmuir (eqn (1)) Freundlich (eqn (2) and (3)), Dubinin–Raduskevich–Kangager (eqn (4)–(6)) and Temkin (eqn (7)) models.³⁶

$$\frac{C_e}{q_e} = \frac{1}{bQ_m} + \frac{C_e}{Q_m}, \quad (1)$$

$$q_e = K_f C_e^{1/n}, \quad (2)$$

$$\log q_e = \log K_f + \frac{1}{n} \log C_e, \quad (3)$$

$$\ln q_e = \ln q_{(D-R)}(-\beta \varepsilon^2), \quad (4)$$

$$\varepsilon = RT \ln \left(1 + \frac{1}{C_e} \right), \quad (5)$$

$$E = \frac{1}{\sqrt{2\beta}}, \quad (6)$$

$$q_e = k_1 \ln(k_2) + k_1 \ln C_e, \quad (7)$$

where q_e is the amount of adsorbed Cr^{6+} (mg g^{-1}), C_e is the equilibrium concentration (mg L^{-1}), b is the adsorption equilibrium constant (L mg^{-1}), Q_m (mg g^{-1}) is the maximum



adsorption capacity for the Langmuir model, K_f is Freundlich constants ($\text{mg g}^{-1} (\text{L mg}^{-1})^{1/n}$) and n is heterogeneity factor, representing the adsorption capacity and the adsorption intensity, respectively. $q_{(\text{D-R})}$ is the theoretical adsorption capacity (mg g^{-1}), β is a constant related to adsorption energy for a mole of the adsorbate ($\text{mol}^2 \text{kJ}^{-2}$), R is the ideal gas constant ($0.008314 \text{ kJ K}^{-1} \text{ mol}^{-1}$), T is the absolute temperature (K), E (kJ mol^{-1}) is the mean free energy per molecule of adsorbate when it transfers from the bulk of the solution (infinity) to the adsorbent surface, k_1 and k_2 are Temkin constants, where k_1 is related to the heat of adsorption (J mol^{-1}) and k_2 is the equilibrium binding constant (L g^{-1}).

The adsorption thermodynamics of α -FeOOH and Fe_3O_4 was determined at the temperatures of 25°C , 40°C and 60°C using 1 ppm Cr^{6+} solution and 0.02 g of each adsorbent. The effects of different initial Cr^{6+} concentrations ($1\text{--}20 \text{ ppm}$), adsorbent doses ($0.02\text{--}0.1 \text{ g}$), and contact times ($10\text{--}90 \text{ min}$) in the Cr adsorption efficiency were investigated. The optimization of pH for Cr^{6+} removal was conducted in the range of $1\text{--}7$, which covers the point of zero charges (PZC) of both adsorbents.

The stability and adsorption behavior of Cr species on adsorbent surfaces were investigated by performing a reusability test. Each adsorbent was separated from the solution and dried overnight at 50°C before starting a new cycle.

Results and discussion

Structures of α -FeOOH and Fe_3O_4

The crystal structures of as-synthesized and Cr-adsorbed Fe_3O_4 and α -FeOOH were determined by XRD as shown in Fig. 1a and

b, respectively. The XRD pattern of α -FeOOH indicated its orthorhombic structure. The lattice constants of α -FeOOH structure were calculated as $a = 4.611 \text{ \AA}$, $b = 9.962 \text{ \AA}$, $c = 3.024 \text{ \AA}$ (JCPDS no. 29-0713).^{37,38} The diffraction pattern of Fe_3O_4 indicated its cubic structure (JCPDS no. 19-0629)^{28,39} with a lattice constant of $a = b = c = 8.364 \text{ \AA}$. The phase indexing and the refined unit cell parameters were reported in ESI data S1† and their corresponding XRD refinement in S2–S5.† Specifically, the Fe_3O_4 and $\text{Cr}@ \text{Fe}_3\text{O}_4$ samples were indexed as magnetite Fe_3O_4 phase (cubic, space group $Fd\bar{3}m$), while the α -FeOOH and $\text{Cr}@ \alpha$ -FeOOH samples were indexed as iron (iii) oxide hydroxide goethite phase (orthorhombic, space group $Pbnm$).

A closer inspection of the refinement results, the addition of chromium species into the materials led to a slight shrinkage of the unit cell parameters compared to the pristine materials. This observation suggested the incorporation of Cr^{3+} into the material matrix of Fe_3O_4 (or FeOOH) without the presence of an additional crystalline impurity phase. In these cases, the atomic site occupancy could not be precisely defined. In addition, XAS was used to propose the local structures of Cr and Fe species in the obtained materials.

The TEM images and lattice parameters of α -FeOOH and Fe_3O_4 are displayed in Fig. 2. The α -FeOOH exhibited short-range-order and rod-like structures (Fig. 2a). The selected area electron diffraction (SAED) pattern of rod-like particles confirmed the orthorhombic structure of α -FeOOH with the (130) and (061) characteristic planes. Its particle size was in the range of $620 (\pm 219) \times 55 (\pm 21) \text{ nm}$ as shown in S6.† The TEM image of Fe_3O_4 in Fig. 2b revealed spherical particles of $400 \pm 124 \text{ nm}$ with characteristic planes of (311) and (422).³³ The BET surface areas of α -FeOOH and Fe_3O_4 were $84 \text{ m}^2 \text{ g}^{-1}$ and $32 \text{ m}^2 \text{ g}^{-1}$, respectively. The larger particle size of Fe_3O_4 led to a lower surface area.

Cr-adsorption ability

Effect of pH. The PZC values of Fe_3O_4 and α -FeOOH were 5.95 ± 0.04 and 3.95 ± 0.06 , respectively (S7†). The Cr-adsorption dependency on pH is shown in Fig. 3. When $\text{pH} < \text{PZC}$, surfaces of Fe_3O_4 and α -FeOOH are protonated to a positive charge. Thus, the adsorption behavior of Fe_3O_4 and α -FeOOH is facilitated by an electrostatic mechanism with negative Cr-compounds (HCrO_4^- , CrO_4^{2-} , and $\text{Cr}_2\text{O}_7^{2-}$).⁴⁰ The adsorbent surface does not favor Cr^{6+} adsorption with a pH increase.⁴¹ The highest Cr-adsorption ability of both adsorbents was detected at $\text{pH} = 3$.

Fe_3O_4 had a higher Cr-adsorption ability than α -FeOOH, indicating its stronger attraction to the negative compounds of Cr^{6+} . Thus, $\text{pH} = 3$ was selected as the optimized value to reach the maximum capacity of the adsorbents. The maximum Cr^{6+} uptakes by α -FeOOH and Fe_3O_4 were determined as about 2.08 mg g^{-1} and 2.87 mg g^{-1} , respectively. In addition, the effects of adsorbent dose, initial concentration and contact time of Cr-adsorption were discussed in S8–S10.†

Adsorption behavior of Fe_3O_4 and α -FeOOH

Adsorption kinetics. The kinetic parameters of Cr^{6+} adsorption on α -FeOOH and Fe_3O_4 are summarized in S13.† The given

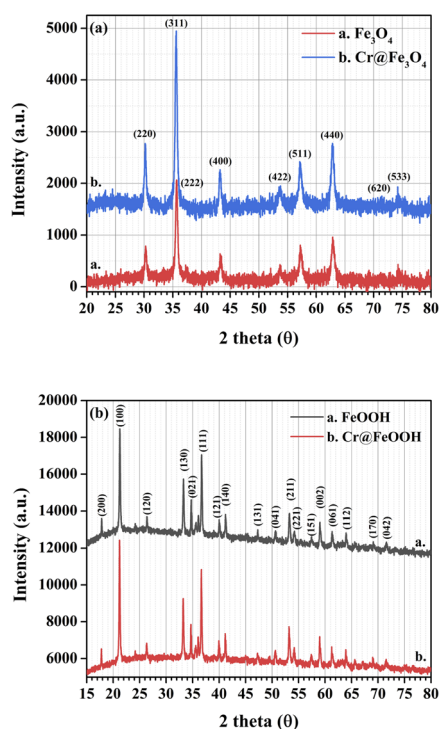


Fig. 1 XRD patterns of as-synthesized and Cr-adsorbed (a) Fe_3O_4 and (b) α -FeOOH.



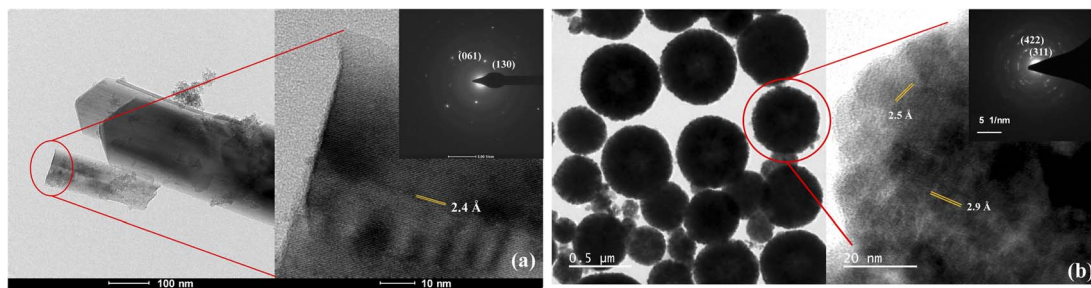


Fig. 2 TEM images of (a) α -FeOOH and (b) Fe_3O_4 .

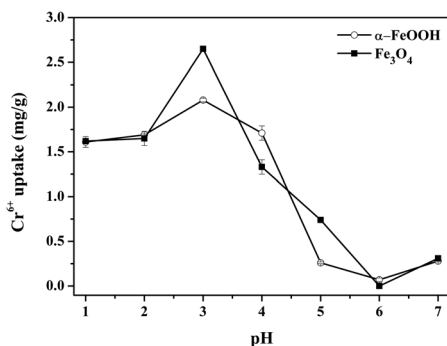


Fig. 3 Effect of pH on Cr^{6+} uptake by the Fe_3O_4 and α -FeOOH adsorption condition: Cr^{6+} initial concentration = 1 ppm, adsorbent dose = 0.4 g L^{-1} , time = 30 min.

correlation coefficient (R^2) of the adsorbents obeyed the pseudo-second order model. The model implies that the rate law for adsorption is described in terms of an initial concentration of Cr rather than in terms of adsorbent concentration. In addition, the chemisorption process is implicated in a rate-determining step of Cr on both ion-oxides.^{45,46}

Adsorption thermodynamics. Adsorption isotherms were fitted based on the Langmuir and Freundlich, Dubinin–Raduskevich–Kanager and Temkin models (S11[†]), and the corresponding fitting parameters and correlation coefficients are listed in S12.[†] The Cr^{6+} adsorption behaviors of α -FeOOH and Fe_3O_4 obeyed the Langmuir model (higher regression coefficient (R^2)) indicating that adsorption takes place at a specific homogeneous site, and monolayer coverage was formed on the adsorbent surface.^{42–44} A low b value implied a strong binding ability.²⁸ Therefore, the lower b value of Fe_3O_4 indicated its stronger Cr^{6+} adsorption ability than that of α -FeOOH.

The thermodynamic parameters of α -FeOOH and Fe_3O_4 are listed in S14.[†] Gibb's free energy changes (ΔG°) for both adsorbents had negative values, confirming a spontaneous nature of adsorption.³⁴ An α -FeOOH had a negative standard enthalpy change (ΔH°) implying an exothermic process.⁴⁷ α -FeOOH had a negative entropy change (ΔS°) indicating the decreased randomness at the solid/solution interface.⁴⁸ In contrast, Fe_3O_4 showed an endothermic process from a positive ΔH° value indicating that an ion-exchange on the adsorbent

surface might occur.⁴⁹ The positive ΔS° of Fe_3O_4 implied randomness at the solid–solution interface during the adsorption process due to adsorption and subsequent desorption.⁴⁸

The reusability of both adsorbents for five cycles is shown in Fig. 4 to support the thermodynamic hypothesis of α -FeOOH and Fe_3O_4 . Different adsorption behaviors of the adsorbents were exhibited. The Cr^{6+} uptake of Fe_3O_4 dramatically decreased (90–95%) in the subsequent cycles. On the other hand, the Cr^{6+} uptake of α -FeOOH slowly decreased by 55–60% in the subsequent cycles. These results implied that the Fe_3O_4 surface was completely adsorbed by Cr-species and it was difficult to detach from the surface. In contrast, the α -FeOOH surface was weakly adsorbed by the adsorbent due to a weak interaction (physisorption) which probably detached from the surface.

Analysis of the adsorbed species on adsorbents

Surface analysis of α -FeOOH and Fe_3O_4 by XPS. The oxidation states of surface elements in the pristine and Cr-adsorbed adsorbents were analyzed by XPS (Fig. 5). The C 1s peak at 284.8 eV was used as a reference to correct electrostatic charging. The binding energies of Fe 2p_{3/2} and Fe 2p_{1/2} in Fig. 5a and b corresponded to Fe_3O_4 and α -FeOOH. The peaks of octahedral Fe^{2+} , octahedral Fe^{3+} , and tetrahedral Fe^{3+} at 710.7 eV, 711.7 eV, and 714.1 eV were determined in the pristine Fe_3O_4 sample corresponded to the typical Fe_3O_4 structure. The corresponding energies of Cr@ Fe_3O_4 were found at 710.3 eV, 711.7 eV, and 713.9 eV, respectively, which were slightly lower

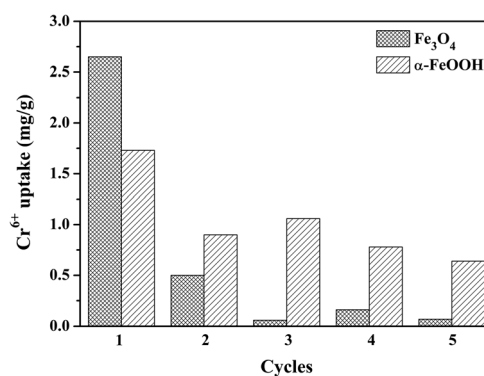


Fig. 4 Reusability for Cr^{6+} removal of Fe_3O_4 and α -FeOOH adsorbents with Cr^{6+} initial concentration = 1 ppm, adsorbent dose = 0.4 g L^{-1} , pH = 3, time = 30 min.



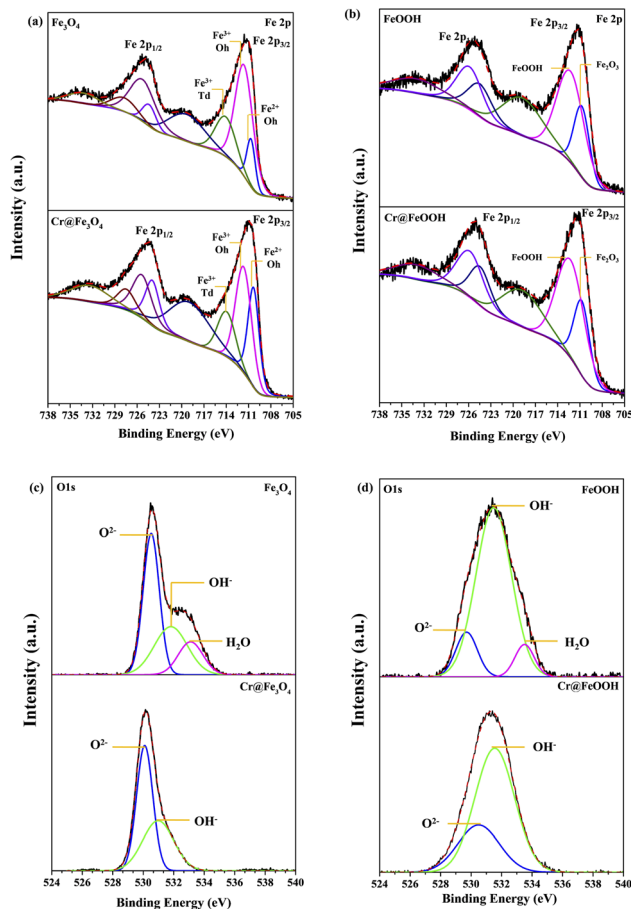


Fig. 5 Fe 2p XPS spectra before and after Cr⁶⁺ adsorption of (a) Fe₃O₄ and (b) α-FeOOH and O 1s spectra before and after Cr⁶⁺ adsorption of (c) Fe₃O₄ and (d) α-FeOOH.

than those of the pristine Fe₃O₄. In addition, the area ratio of Fe²⁺_{Oh}/Fe³⁺_{Oh} in Cr@Fe₃O₄ was higher than the pristine Fe₃O₄. The result indicated a decrease of Fe³⁺_{Oh} in Fe₃O₄ after Cr-adsorption. The Fe 2p energies at 710.7 eV and 712.3 eV corresponding to Fe₂O₃ and α-FeOOH components, respectively, were observed on both the pristine α-FeOOH and Cr@FeOOH.⁵⁰ It was implied that surface species of α-FeOOH were not changed after Cr-adsorption.

The O 1s peaks of pristine Fe₃O₄ at 530.5 eV, 531.8 eV, and 533.1 eV appeared from lattice oxygen (O²⁻_{lattice}), oxygen in the adsorbed-hydroxyl group (OH_{ads}), and oxygen in water-adsorbed molecules (H₂O_{ads}), respectively (Fig. 5c and d). After Cr adsorption, the binding energies of O²⁻_{lattice} and OH_{ads} slightly decreased to 530.1 eV and 530.9 eV, respectively, indicating a presence of O²⁻_{lattice} in CrO(OH) over the Fe₃O₄ surface.^{51–53} The results exhibited a partial ion-exchange Cr³⁺ in Fe³⁺ sites which well corresponded to the decrease of Fe³⁺_{Oh} constituent as mentioned in the Fe 2p energy. Moreover, no peak corresponding to water-adsorbed species on Cr@Fe₃O₄ was determined because Cr-adsorbed species fully covered the Fe₃O₄ surface. The O 1s peaks of α-FeOOH at 530.5, 530.5 and 531.5 eV corresponded to O²⁻_{lattice}, OH_{ads} and adsorbed H₂O species, respectively. The adsorbed H₂O was not determined on Cr@FeOOH. In addition, the binding energy of O²⁻_{lattice} in

Cr@FeOOH was slightly higher than that in α-FeOOH. These results possibly indicate the presence of precipitate oxide form of Cr₂O₃ on the α-FeOOH surface.

The binding energies of Cr 2p_{3/2} and Cr 2p_{1/2} in Cr@Fe₃O₄ and Cr@α-FeOOH are shown in Fig. 6. The Cr 2p_{3/2} to Cr 2p_{1/2} splitting energies of both samples were about 10 eV which was typically found in a Cr³⁺/Cr⁶⁺ mixture.⁵⁴ The Cr 2p_{3/2} exhibited the characteristics of Cr³⁺ in Cr₂O₃ (576.6 eV), CrO(OH)/Cr(OH)₃ (577.7 eV) and Cr⁶⁺ in CrO₃ (579.9 eV).^{7,42,44,50–54} Those characters were similarly found in Cr@Fe₃O₄ and Cr@FeOOH. However, the area ratio of Cr₂O₃/CrO(OH) in Cr@FeOOH was higher than that in Cr@Fe₃O₄. The finding correlated with the enhancement of O²⁻_{lattice} species of Cr@FeOOH in O 1s spectrum. This result revealed the presence of precipitated Cr₂O₃ species on the α-FeOOH surface at pH 3.⁵⁵ It was noticeable that a high CrO(OH) content in Cr@Fe₃O₄ might proceed through Cr³⁺ migration on the Fe₃O₄ surface.

Bulk analysis of α-FeOOH and Fe₃O₄ by XAS

XANES of Fe K-edge and L₃-edge. The Fe K-edge spectra of Fe₃O₄ and α-FeOOH compared with the iron oxide standards are shown in Fig. 7. The Fe K-edge energy of the pristine Fe₃O₄ was calculated as 7120.7 eV while the energy of Cr@Fe₃O₄ slightly shifted to a lower value of 7120.5 eV. This result indicated that ferrous specie (Fe²⁺) in Fe₃O₄ increased after Cr-adsorption. On the other hand, the Fe K-edge energies of the pristine α-FeOOH and Cr@FeOOH were similar (Fig. 7b). Thus, the bulk structure of α-FeOOH was not affected by Cr-adsorption process.

In principle, Fe L₃-edge has a better resolution for fine structures and manifests a lower intrinsic lifetime broadening than Fe K-edge. Thus, the local geometry of Fe₃O₄ was further investigated by Fe L₃-edge. The spectra of Fe₃O₄ and Cr@Fe₃O₄ are presented in Fig. 7c. The I_a/I_b intensity ratio in the Fe L₃-edge spectrum was used to determine the mixed valence state.⁵⁶ The Cr@Fe₃O₄ had I_a/I_b ratio of 0.59 which was higher than that of pristine Fe₃O₄ (0.53). The higher I_a/I_b intensity ratio

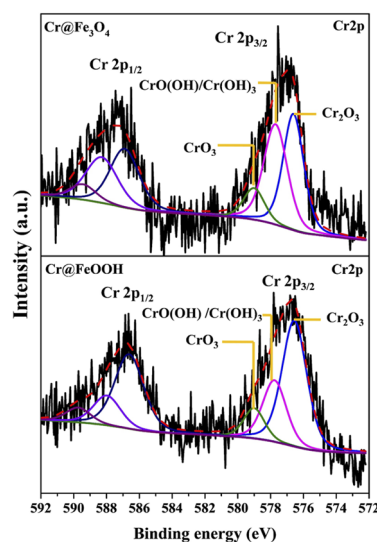


Fig. 6 Cr 2p XPS spectra of Cr@Fe₃O₄ and Cr@FeOOH.



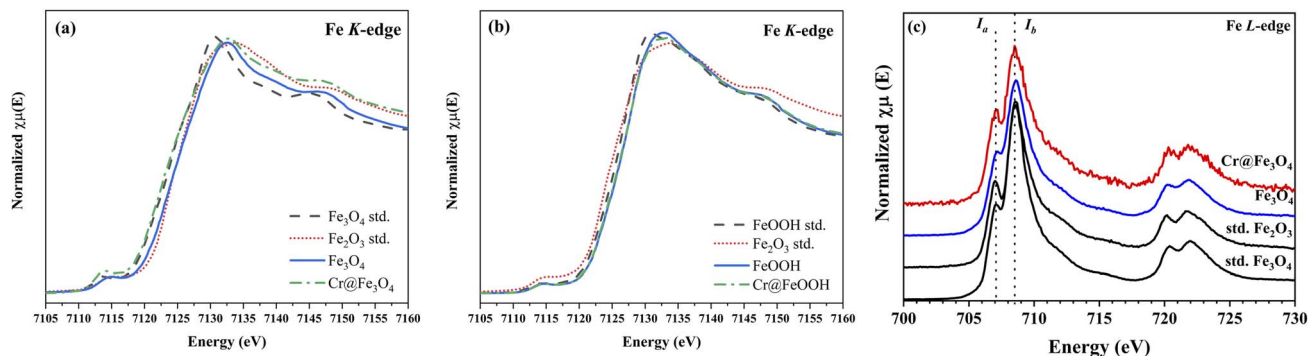


Fig. 7 Fe K-edge XANES spectra of bare and Cr-adsorbed (a) Fe_3O_4 and (b) $\alpha\text{-FeOOH}$ and (c) Fe L_3 -edge XANES spectra of $\text{Cr@Fe}_3\text{O}_4$ and Cr@FeOOH comparing with the iron standards.

corresponded to the lower Fe^{2+} content in the tetrahedral site of Fe_3O_4 .⁵⁶

XANES of Cr K-edge. A comparison of Cr K-edge in the Cr-adsorbed samples with CrCl_3 (Cr^{3+}) and $\text{K}_2\text{Cr}_2\text{O}_7$ (Cr^{6+}) standards are shown in Fig. 8. The Cr^{6+} (4-fold Cr–O) character was exhibited by a strong pre-edge intensity at 5999 eV.⁵⁷ Besides, a weak pre-edge intensity was found in Cr^{3+} (6-fold Cr–O). XANES profile of $\text{Cr@Fe}_3\text{O}_4$ explored a reduction of pre-edge intensity compared with the Cr^{6+} standard. Thus, the Fe_3O_4 could partially reduce Cr^{6+} -species (HCrO_4^- , CrO_4^{2-} , $\text{Cr}_2\text{O}_7^{2-}$) to Cr^{3+} on the surface under aqueous solution at pH 3. This behavior was also observed on Cr@FeOOH .⁵⁸ However, a decrease in pre-edge intensity of Cr@FeOOH was much lower than that of $\text{Cr@Fe}_3\text{O}_4$. Furthermore, Cr^{6+} was a major species in the solution after adsorption (S15[†]).

XANES of O K-edge. The O K-edge XANES spectra and their derivative plots of the pristine and Cr-adsorbed Fe_3O_4 and $\alpha\text{-FeOOH}$ structures are exhibited in Fig. 9. The O K-edge energy of $\text{Cr@Fe}_3\text{O}_4$ (Fig. 9a) shifted to higher values compared to pristine Fe_3O_4 . The result revealed a decrease in the electron density of oxygen atoms in the bulk structure of $\text{Cr@Fe}_3\text{O}_4$. This finding was probably due to an enhancement of oxygen bonding with a higher ionic strength species of Fe^{3+} rather than Fe^{2+} . Hence, an increase of Fe^{3+} –O component in the $\text{Cr@Fe}_3\text{O}_4$ structure was suggested. An increase of Fe^{3+} species in $\text{Cr@Fe}_3\text{O}_4$ was in good agreement with Fe K-edge XANES. In addition, on Fig. 9b, O K-edge energy of $\text{Cr@Fe}_3\text{O}_4$ nearly fitted to $\alpha\text{-FeOOH}$. Thus,

a part of FeO(OH) as well as CrO(OH) could be created on the Fe_3O_4 structure after Cr-adsorption. Meanwhile, the O K-edge energies of $\alpha\text{-FeOOH}$ and Cr@FeOOH were similar indicating no structural change in the bulk structure of $\alpha\text{-FeOOH}$ during Cr adsorption.

EXAFS analysis of Fe and Cr K-edge

EXAFS of Fe K-edge. The local structures of Fe_3O_4 and $\text{Cr@Fe}_3\text{O}_4$ were investigated by Fe K-edge EXAFS analysis. The EXAFS analysis is reported in Table 1 and S16.[†] The 4-fold and 2-fold Fe–O bonds with distances of 1.61 Å and 1.89 Å, respectively, were observed in bare Fe_3O_4 . The bond length of 1.61 Å was shorter than the typical tetrahedral Fe–O bond length in Fe_3O_4 (1.88 Å) due to the existence of oxygen vacancies.⁵⁹ The second shell of the Fe_3O_4 structure consisted of Fe–O (3.14 Å) and Fe–Fe (3.47 Å) bonds. After Cr adsorption, the first shell represented 2-fold (1.97 Å) and 4-fold (2.40 Å) of Fe–O bonds. The bond distances fitted well with octahedral Fe–O in Fe_2O_3 or tetrahedral Fe–O in $\alpha\text{-FeOOH}$. For $\alpha\text{-FeOOH}$, the first shell consisted of tetrahedral Fe–O bonds with an average bond distance of 1.97 Å (Table 1). Moreover, 3-fold Fe–Fe bonds with bond distances of 3.00 Å and 3.30 Å were also displayed. Octahedral Fe–O (1.98 Å) and Fe–Fe (3.00 Å) bonds in Cr@FeOOH were similar to $\alpha\text{-FeOOH}$. Thus, the bulk structure of $\alpha\text{-FeOOH}$ did not change after Cr adsorption.

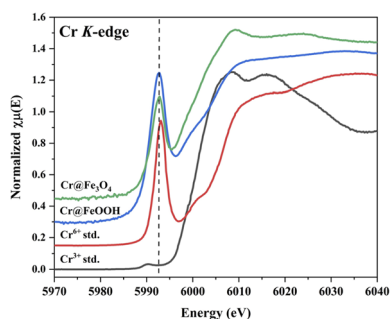


Fig. 8 Cr K-edge XANES spectra of $\text{Cr@Fe}_3\text{O}_4$ and Cr@FeOOH comparing with Cr-standards.

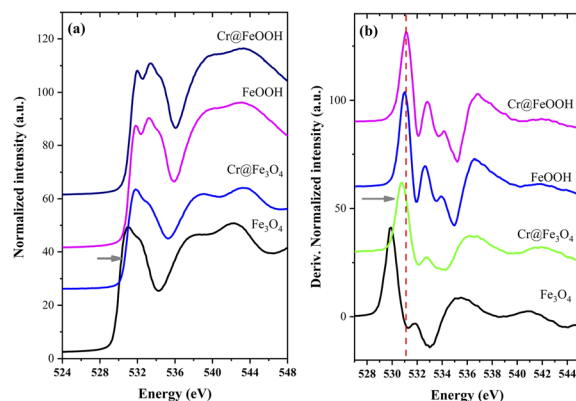


Fig. 9 O K-edge XANES spectra (a) and their derivatives (b) of bare and Cr-adsorbed Fe_3O_4 and $\alpha\text{-FeOOH}$.



Table 1 $k^2(\chi)$ weight of Fe *K*-edge EXAFS of bare and Cr-adsorbed Fe_3O_4 and $\alpha\text{-FeOOH}$

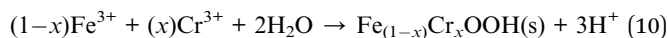
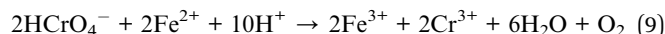
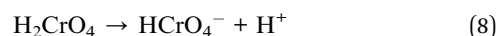
| Sample | Bond | Distance (Å) | Coordination number (CN) | Debye-Waller factor (σ^2) |
|----------------------------|-------|--------------|--------------------------|------------------------------------|
| Fe_3O_4 | Fe–O | 1.61 | 3.9 | 0.054 |
| | Fe–O | 1.89 | 2.8 | 0.006 |
| | Fe–O | 3.14 | 12.0 | 0.048 |
| | Fe–Fe | 3.47 | 12.0 | 0.013 |
| $\text{Cr@Fe}_3\text{O}_4$ | Fe–O | 1.97 | 2.2 | 0.012 |
| | Fe–O | 2.40 | 3.8 | 0.059 |
| | Fe–Fe | 2.76 | 0.9 | 0.004 |
| | Fe–Fe | 3.00 | 2.9 | 0.008 |
| | Fe–Fe | 3.49 | 3.2 | 0.013 |
| $\alpha\text{-FeOOH}$ | Fe–O | 1.97 | 4.3 | 0.012 |
| | Fe–Fe | 3.00 | 3.1 | 0.012 |
| | Fe–Fe | 3.30 | 3.0 | 0.013 |
| | Fe–O | 3.40 | 3.0 | 0.002 |
| | Fe–Fe | 3.89 | 12.0 | 0.035 |
| Cr@FeOOH | Fe–O | 1.98 | 6.0 | 0.013 |
| | Fe–Fe | 3.00 | 6.0 | 0.017 |
| | Fe–O | 3.32 | 6.0 | 0.003 |
| | Fe–O | 3.81 | 12.0 | 0.004 |

EXAFS of Cr *K*-edge. The Cr *K*-edge EXAFS spectrum of $\text{Cr@Fe}_3\text{O}_4$ is displayed in Fig. 10a. Cr–O bonds consisted of short Cr^{6+} –O bonds (1.22 Å and 1.56 Å) and long Cr^{3+} –O bonds (1.87 Å) (Table S17[†]).²⁹ Hence, mixed phases of $\text{Cr}_2\text{O}_3/\text{CrOOH}$ (Cr^{3+}) and CrO_3 (Cr^{6+}) were formed on $\text{Cr@Fe}_3\text{O}_4$. Moreover, 2-fold Cr–Cr bonds of 2.41 Å and 3.62 Å correlated to binuclear $\text{Cr}_2\text{O}_7^{2-}$ species which could be physisorbed on the adsorbent in an aqueous solution at pH 3.

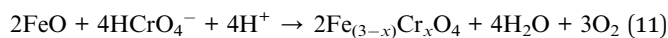
The Cr *K*-edge EXAFS analysis of Cr@FeOOH are presented in Fig. 10b and Table S17.[†] Tetrahedral Cr–O bonds with the bond distances of 1.33 Å and 1.59 Å corresponded to Cr^{6+} in HCrO_4^- . Moreover, the average bond distance of 2-fold Cr–Cr bonds of 3.17 Å was found in Cr@FeOOH which was different from Cr–Cr bonds in $\text{Cr@Fe}_3\text{O}_4$ confirming that the HCrO_4^- species was presented on $\alpha\text{-FeOOH}$.

Removal mechanism of Cr^{6+} on Fe_3O_4 and $\alpha\text{-FeOOH}$. In the solution pH 2.0–6.5, Cr^{6+} in an aqueous solution existed as a predominant form of HCrO_4^- (eqn (8)). This species moved and adsorbed on the surface of both adsorbents. Some Cr^{6+} was reduced to Cr^{3+} or precipitated on surfaces which confirmed by the

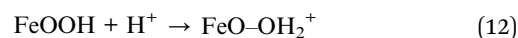
existence of Cr_2O_3 , $\text{CrO}(\text{OH})/\text{Cr}(\text{OH})_3$ and CrO_3 from XPS surface analysis. Compared with $\alpha\text{-FeOOH}$, the lower $\text{Cr}_2\text{O}_3/\text{CrO}(\text{OH})$ ratio in $\text{Cr@Fe}_3\text{O}_4$ implied the Cr-ion migration into the bulk structure of Fe_3O_4 . XANES and EXAFS as bulk analysis further revealed this behavior. The contained Fe^{2+} species inside Fe_3O_4 could reduce Cr^{6+} in HCrO_4^- to Cr^{3+} (eqn (9)) with a relatively slow reaction rate due to the limited electron transfer rate in the maghemite (Fe_2O_3) passivation layer.³⁰ Then, Cr^{3+} species migrated to bulk Fe_3O_4 and formed $\text{Fe}_{(1-x)}\text{Cr}_x\text{OOH}$ containing Fe^{3+} and Cr^{3+} in between FeO lattice (eqn (10)). These dissolved octahedral Cr^{3+} –O sites could prevent the bulk structure of Fe_3O_4 from collapsing.^{60,61}



Additionally, the XPS and XAS results revealed the increase of FeO species in Fe_3O_4 after Cr-adsorption. Thus, the most likely form was a $\text{Fe}_{(3-x)}\text{Cr}_x\text{O}_4$ solid solution containing Fe^{2+} and Cr^{3+} in forms of FeO and Cr_2O_3 .⁶² The presented species might be created through Cr^{6+} reduction mechanism by FeO in Fe_3O_4 (or $\text{FeO}\cdot\text{Fe}_2\text{O}_3$) structure as expressed by eqn (11).



Meanwhile, $\alpha\text{-FeOOH}$ surface changed to positive $[\text{FeO}-\text{OH}_2]^{2+}$ species at pH = 3.0 (eqn (12)). These $[\text{FeO}-\text{OH}_2]^{2+}$ molecules could react with the presented negative HCrO_4^- species by an electrostatic force (physisorption) and created $\text{FeO}-\text{HCrO}_4$ species (eqn (13)).⁷ This adsorption behavior did not change the local geometry and oxidation state of iron atoms in $\alpha\text{-FeOOH}$.



Conclusions

Fe_3O_4 (magnetite) and $\alpha\text{-FeOOH}$ (goethite) synthesized by the hydrothermal method were mainly in cubic and orthorhombic structures, respectively. The Cr adsorption isotherms of Fe_3O_4 and $\alpha\text{-FeOOH}$ fitted well with the Langmuir model, indicating a monolayer adsorption process. The maximum Cr^{6+} uptake of 2.87 mg g^{-1} was found by Fe_3O_4 . After Cr-adsorption, the Cr^{3+} -doped forms of $\text{Fe}_{(1-x)}\text{Cr}_x\text{OOH}$ and $\text{Fe}_{(3-x)}\text{Cr}_x\text{O}_4$ solid solution was observed in bulk Fe_3O_4 resulting in a high Cr-adsorption capacity. Besides, an electrostatic attraction of $\text{FeO}-\text{HCrO}_4$ occurred only on the $\alpha\text{-FeOOH}$ surface leading to a low Cr-adsorption capacity. The Cr-adsorption ability and behavior in an aqueous solution of the adsorbents were strongly influenced by an adsorbed species stabilized on their structures. The discovered Cr-solid solution in Fe_3O_4 could be a promising catalyst preparation through water treatment process.

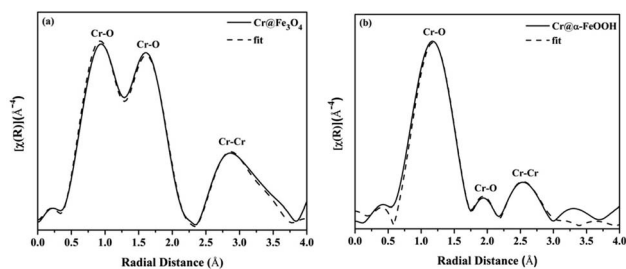


Fig. 10 Fourier transforms of the $k^3(\chi)$ weighted in Cr *K*-edge EXAFS data collected from (a) $\text{Cr@Fe}_3\text{O}_4$ and (b) Cr@FeOOH .



Author contributions

Nichapha Senamart-data curation, formal analysis, writing-original draft, writing-review & editing; Krittanun Deekamwong-writing-review & editing; Jatuporn Wittayakun-supervision & editing; Sanchai Prayoonpokarach-review & editing; Narong Chanlek-data analysis; Yingyot Poo-arporn-review & editing; Suttipong Wannapaiboon-data curation, formal analysis, writing; Pinit Kidkhunthod-data analysis and Sirinuch Loiha-conceptualization, funding acquisition, supervision, writing-review & editing.

Conflicts of interest

There are no conflicts to declare.

Acknowledgements

This work was supported by the Science Achievement Scholarship of Thailand (SAST), Center for Innovation in Chemistry (PERCH-CIC), Materials Chemistry Research Center (MCRC), Thailand. Department of Chemistry, Faculty of Science, Khon Kaen University, Khon Kaen, Thailand. Research and Graduate Studies Department, KKU (Research Program, grant number RP64-6/001), fiscal year 2021. Synchrotron Light Research Institute (SLRI), Nakhon Ratchasima, Thailand (BL1.1W, BL2.2, BL3.2Ua, BL5.2 and BL5.3). Suranaree University of Technology (SUT), Thailand Science Research and Innovation (TSRI), and National Science, Research and Innovation Fund (NSRF) (90464/project code 90464).

References

- 1 A. Chiu, X. L. Shi, W. K. P. Lee, R. Hill, T. P. Wakeman, A. Katz, B. Xu, N. S. Dalal, J. D. Robertson, C. Chen, N. Chiu and L. Donehower, *J. Environ. Sci. Health, Part C: Environ. Carcinog. Ecotoxicol. Rev.*, 2010, **28**, 188–230.
- 2 M. Narayani and K. V. Shetty, *Crit. Rev. Environ. Sci. Technol.*, 2012, **43**, 955–1009.
- 3 R. Rakhunde, L. Deshpande and H. D. Juneja, *Crit. Rev. Environ. Sci. Technol.*, 2011, **42**, 776–810.
- 4 E. J. Tomaszewski, S. Lee, J. Rudolph, H. Xu and M. Ginder-Vogel, *Chem. Geol.*, 2017, **464**, 101–109.
- 5 L. Li, Y. Li, L. Cao and C. Yang, *Carbohydr. Polym.*, 2015, **125**, 206–213.
- 6 P. Lazo, *J. Int. Environ. Appl. Sci.*, 2009, **4**, 207–213.
- 7 S. Wu, J. Lu, Z. Ding, N. Li, F. Fu and B. Tang, *RSC Adv.*, 2016, **6**, 82118–82130.
- 8 S. R. Chowdhury, E. K. Yanful and A. R. Pratt, *J. Hazard. Mater.*, 2012, **235–236**, 246–256.
- 9 X. Lv, J. Xu, G. Jiang, J. Tang and X. Xu, *J. Colloid Interface Sci.*, 2012, **369**, 460–469.
- 10 Y. L. Wei, Y. C. Lee and H. F. Hsieh, *Chemosphere*, 2005, **61**, 1051–1060.
- 11 A. H. Meena and Y. Arai, *Geochem. Trans.*, 2016, **17**, 1.
- 12 M. Gheju and I. Balcu, *J. Hazard. Mater.*, 2011, **196**, 131–138.
- 13 A. Maleki, B. Hayati, M. Naghizadeh and S. W. Joo, *J. Ind. Eng. Chem.*, 2015, **28**, 211–216.
- 14 M. Gheju, *Water, Air, Soil Pollut.*, 2011, **222**, 103–148.
- 15 S. M. El-Sheikh, A. B. Azzam, R. A. Geioushy, F. M. El Dars and B. A. Salah, *J. Alloys Compd.*, 2021, **857**, 157513.
- 16 R. A. Geioushy, S. M. El-Sheikh, A. B. Azzam, B. A. Salah and F. M. El-Dars, *J. Hazard. Mater.*, 2020, **381**, 120955.
- 17 F. Di Natale, A. Erto, A. Lancia and D. Musmarra, *J. Hazard. Mater.*, 2015, **281**, 47–55.
- 18 S. M. Lee, L. Lalchhingpuii and D. Tiwari, *Chem. Eng. J.*, 2016, **296**, 35–44.
- 19 Q. Liu, Q. Liu, W. Ma, W. Liu, X. Cai and J. Yao, *Colloids Surf., A*, 2016, **511**, 8–16.
- 20 E. I. Basaldella, P. G. Vázquez, F. Iucolano and D. Caputo, *J. Colloid Interface Sci.*, 2007, **313**, 574–578.
- 21 L. N. Døssing, K. Dideriksen, S. L. S. Stipp and R. Frei, *Chem. Geol.*, 2011, **285**, 157–166.
- 22 D. L. Sedlak and P. G. Chan, *Geochim. Cosmochim. Acta*, 1997, **61**, 2185–2192.
- 23 A. E. Gleason, R. Jeanloz and M. Kunz, *Am. Mineral.*, 2008, **93**, 1882–1885.
- 24 H. Abdel-Samad and P. R. Watson, *Appl. Surf. Sci.*, 1997, **108**, 371–377.
- 25 T. Mineno and M. Okazaki, *Soil Sci. Plant Nutr.*, 2004, **50**, 1043–1046.
- 26 V. D. Nguyen, J. Kynicky, P. Ambrozova and V. Adam, *Materials*, 2017, **10**, 783.
- 27 M. Kumari, C. U. Pittman Jr and D. Mohan, *J. Colloid Interface Sci.*, 2014, **442**, 120–132.
- 28 S. Rajput, C. U. Pittman and D. Mohan, *J. Colloid Interface Sci.*, 2016, **468**, 334–346.
- 29 A. H. Meena and Y. Arai, *Geochem. Trans.*, 2016, **17**, 1.
- 30 J. Chang, H. Wang, J. Zhang, Q. Xue and H. Chen, *Colloids Surf., A*, 2021, **611**, 125784.
- 31 N. Senamart, J. Watcharakitti, K. Atthawilai, K. Phedluen, P. Nasomjai and S. Loiha, *Suranaree J. Sci. Technol.*, 2018, **25**, 445–454.
- 32 P. Ou, G. Xu, Z. Ren, X. Hou and G. Han, *Mater. Lett.*, 2008, **62**, 914–917.
- 33 U. Pal, S. Uribe Madrid and F. Sanchez De-jesus, *Adv. Nano. Res.*, 2014, **2**, 187–198.
- 34 G. Du, Z. Li, L. Liao, R. Hanson, S. Leick, N. Hoepfner and W. T. Jiang, *J. Hazard. Mater.*, 2012, **221–222**, 118–123.
- 35 M. Kazemi, M. Jahanshahi and M. Peyravi, *J. Hazard. Mater.*, 2018, **344**, 12–22.
- 36 O. Ali and S. K. Mohamed, *Turk. J. Chem.*, 2017, **41**, 967–986.
- 37 F. Geng, Z. Zhao, J. Geng, H. Cong and H.-M. Cheng, *Mater. Lett.*, 2007, **61**, 4794–4796.
- 38 A. R. Amani-Ghadim, S. Alizadeh, F. Khodam and Z. Rezvani, *J. Mol. Catal. A: Chem.*, 2015, **408**, 60–68.
- 39 S. Alibeigi and M. R. Vaezi, *Chem. Eng. Technol.*, 2008, **31**, 1591–1596.
- 40 Y. F. Shen, J. Tang, Z. H. Nie, Y. D. Wang, Y. Ren and L. Zuo, *Sep. Purif. Technol.*, 2009, **68**, 312–319.
- 41 N. Guo, X. Lv, Q. Li, T. Ren, H. Song and Q. Yang, *Microporous Mesoporous Mater.*, 2020, **299**, 110101.



- 42 Z. Liu, G. Chen, L. Xu, F. Hu and X. Duan, *ChemistrySelect*, 2019, **4**, 13817–13827.
- 43 M. Bhaumik, A. Maity, V. V. Srinivasu and M. S. Onyango, *J. Hazard. Mater.*, 2011, **190**, 381–390.
- 44 S. U. N. Zhenya, Z. H. U. Chunshui, H. Jiangbo, G. Wenqi, C. Hesheng and M. U. Shanbin, *Acta Geol. Sin.*, 2006, **80**, 597–603.
- 45 X. Q. Zhang, Y. Guo and W.-C. Li, *RSC Adv.*, 2015, **5**, 25896–25903.
- 46 M. Ahmaruzzaman, *Adv. Colloid Interface Sci.*, 2011, **166**, 36–59.
- 47 G. Vijayakumar, R. Tamilarasan and M. Dharmendirakumar, *J. Mater. Environ. Sci.*, 2012, **3**, 157–170.
- 48 M. Hasanpour and M. Hatami, *Adv. Colloid Interface Sci.*, 2020, **284**, 102247.
- 49 Y. H. Li, Z. Di, J. Ding, D. Wu, Z. Luan and Y. Zhu, *Water Res.*, 2005, **39**, 605–609.
- 50 A. P. Grosvenor, B. A. Kobe, M. C. Biesinger and N. S. McIntyre, *Surf. Interface Anal.*, 2004, **36**, 1564–1574.
- 51 X. Zhang, W. G. Sloof, A. Hovestad, E. P. M. van Westing, H. Terry and J. H. W. de Wit, *Surf. Coat. Technol.*, 2005, **197**, 168–176.
- 52 Z. Wen, J. Ke, J. Xu, S. Guo, Y. Zhang and R. Chen, *Chem. Eng. J.*, 2018, **343**, 416–426.
- 53 Z. Wen, Y. Zhang, S. Guo and R. Chen, *J. Colloid Interface Sci.*, 2017, **486**, 211–218.
- 54 Z. Wen, Y. Zhang, G. Cheng, Y. Wang and R. Chen, *Chemosphere*, 2019, **218**, 1002–1013.
- 55 S. M. Walker, M. C. Marciano, W. M. Bender and U. Becker, *Chem. Geol.*, 2016, **429**, 60–74.
- 56 B. P. von der Heyden, A. N. Roychoudhury, T. Tyliczszak and S. C. B. Myneni, *Am. Mineral.*, 2017, **102**, 674–685.
- 57 S. Ould-Chikh, O. Proux, P. Afanasiev, L. Khrouz, N. Hedhili Mohamed, H. Anjum Dalaver, M. Harb, C. Geantet, J. M. Basset and E. Puzenat, *ChemSusChem*, 2014, **7**, 1361–1371.
- 58 C. J. Keturakis, M. Zhu, E. K. Gibson, M. Daturi, F. Tao, A. I. Frenkel and I. E. Wachs, *ACS Catal.*, 2016, **6**, 4786–4798.
- 59 F. Pinakidou, M. Katsikini, K. Simeonidis, E. Kaprara, E. C. Paloura and M. Mitrakas, *Appl. Surf. Sci.*, 2016, **360**, 1080–1086.
- 60 S.-f. Niu, Y. Liu, X.-h. Xu and Z.-h. Lou, *J. Zhejiang Univ., Sci., B*, 2005, **6**, 1022–1027.
- 61 T. Kendelewicz, P. Liu, C. S. Doyle and G. E. Brown, *Surf. Sci.*, 2000, **469**, 144–163.
- 62 X. Wang, N. Chen and L. Zhang, *Environ. Sci.: Nano*, 2019, **6**, 2185–2194.

